



XRD and UV–Vis studies of cellulose acetate film blended with different concentrations of nano-metal oxide

Dina Ezzat¹ · Mortda Youssif² · Hanan Elhaes³ · Mahmoud El-Nahass⁴

Received: 5 October 2023 / Accepted: 28 January 2024 / Published online: 30 March 2024
© The Author(s) 2024

Abstract

Molybdenum Trioxide nanoparticle (MoO₃-NPs) was introduced to Cellulose acetate (CA) biopolymer with different concentration using casting process by dispersed MoO₃-NPs [0.0, 0.25, 0.5 and 1.0 wt%]. Molecular structure of samples has been studied using XRD and UV–Vis. the data shown by X-ray results indicated the amorphous nature of the pure polymer. Some peaks are appeared as a result of the addition of MoO₃-NPs which indicate that samples were partially crystallized. The crystallite size of nano-metal oxide was calculated for blended samples by Size–Strain Plot method which was found to increase with increasing the concentration of MoO₃. UV–Vis results indicate that there exist two indirect energy band gaps; Onset band gap which observed to decreases from 1.3 eV for pure polymer to 0.78 eV for polymer blended with 1.0 wt% MoO₃-NPs and HOMO–LOMO band gap which observed to decrease from 3.23 eV for pure polymer to 2.89 eV for polymer blended with 1.0 wt% MoO₃-NPs. This indicate that the addition of nano-metal oxide improve the optical conduction of CA. Urbach energy was observed to increase with increasing MoO₃-NPs from 0.27 eV for pure CA to 0.32 eV for 1.0 wt% MoO₃-NPs concentration which may be occurred due to the creation localized states at the band gap as a result of the addition of MoO₃-Nps.

Keywords Cellulose acetate · Size–Strain Plot method · MoO₃-NPs · XRD · UV–vis

✉ Dina Ezzat
Dinae@oi.edu.eg

¹ Obour Institute, Qalyubia, Egypt

² Physics Department, Faculty of Science at New Damietta, Damietta University, New Damietta 34517, Egypt

³ Physics Department, Faculty of Women for Arts, Science, and Education, Ain Shams University, Cairo 11757, Egypt

⁴ Physics Department, Faculty of Education, Ain Shams University, Roxy, Cairo, Egypt

1 Introduction

In the last few years, an interest has been increased in developing polymer-based nanomaterials and nanocomposites. Such materials have technological applications in different areas such as optical and gas sensors, electronic and optoelectronic devices, UV-detectors, pharmaceuticals, medical, food packaging and biological applications (Michalet et al. 2005; Wang et al. 2009, 2011; Li et al. 2012; Mochalin and Gogotsi 2009). Such materials also have been well utilized in environmental conservation and protection (Penget al. 2012; Vimala et al. 2020, 2021; Chabba et al. 2005; Hashmi et al. 2020). Natural green polymers have acted an important role in an environmental conservation. Polysaccharides like cellulose and its derivatives show unique properties dedicating them for many applications (Ibrahim et al. 2011; Ezzat et al. 2020, 2019). Cellulose is the greatest abundant material which make researchers get excited in developing applications. Cellulose acetate (CA) is a thermoplastic polymer produced by treating cellulose. It exhibits additional features as mechanical and thermal resistance, dimensional and thermal stability as well as low cost (Vahid et al. 2022). CA can easily be poured as film, membrane, or sphere. It has many applications either in technology field or in science. It can be used as a support for plastics, fibers, photographic films industries, or pharmaceuticals coating (Orelma et al. 2020; Căprărescu et al. 2020). Introducing inorganic materials into polymers have been suggested so as to increase polymers properties (Vahid et al. 2022). Blending polymer with nanoparticle transition metal oxide is an interesting point of view. The addition of inorganic nanoparticles to polymers enable the modification of many physical properties of polymers. The resulting physical characteristics: thermal, mechanical, optical, magnetic or conducting properties of the nanocomposites are effected by the filler properties and by the fillers surface properties. Specific interest is to construct the polymeric nanocomposite with good thermo-mechanical properties, rheological characteristics and also thermal stability for energy and environmental applications (Hanemann et al. 2010) due to their importance for using in many fields like photonics, optics, electrical and electronics fields (Azelia et al. 2021; pasha et al. 2015; Archana et al 2014; Ramesan et al. 2018; Baeg et al. 2013). Such addition of nanoparticles was observed to enhance polymers properties remarkably which make them used in many applications. catalysts, sensors, lubricants, display devices, smart windows, battery electrodes are some examples for applications (Sivacarendran et al. 2013; Chen et al. 2013; Alghunaim et al. 2017; Badry et al. 2019). Addition of transition metal oxide on the structure and physical characteristic of cellulose acetate was studied (Ezzat et al. 2015; Muhammad et al. 2022; Wang et al.2014). An example of metal oxides that have been used for blending polymer is MoO_3 . Molybdenum trioxide offers many interesting properties. It is the most abundant of all molybdenum compounds. Molybdenum state of oxidation is +6 in MoO_3 compound. Molybdenum trioxide (MoO_3) is one important transition metal oxide which has band gap energy of value 3.15 eV (Muhammad et al. 2023). It has a great field of applications like using in fabricating gas sensors, smart windows, electrochromism, photochromism, imaging devices, heterogeneous catalysis, electro catalysis, field—effect transistors, electrodes of rechargeable batteries, and supported catalysts (Wang et al. 2014; Wongkrua et al. 2013). Molybdenum trioxide still has a broad range of usage such as an adhesive also it used as an additive to industrial material such as steel and corrosion resistant alloys (Fakhri and Nejad 2016). Based on these considerations the present study introduces the preparation and characterization of CA blending with varying concentrations of molybdenum trioxide-nanoparticles (MoO_3 -NPs). Casting method is the simplest film-forming method, it used in preparing samples. It has many advantage

such as no equipment is needed except a very horizontal work surface. The procedure is to simply cast a solution onto a Petri dish then drying. It makes films with good quality and also thick films (Yogamalar et al. 2009; Frederik 2009). The microstructural properties and optical parameters have been studied using XRD, and UV-vis techniques.

2 Material and method

Cellulose acetate and Molybdenum Trioxide nanoparticle were obtained from Aldrich company, Inc., USA. Cellulose acetate with 39.7 wt% of acetyl content. Meanwhile, dimethyl sulphoxide was purchased from Labscan Ltd., Unit. However, CA and CA/MoO₃-NPs blend materials were prepared by casting technique (Ezzat et al. 2021). One gram of CA powder was dissolved in 20 ml of Dimethyl Sulphoxide with (0.0, 0.25, 0.5 and 1.0 wt%) concentrations of MoO₃-NPs. The solution was then stirred under a stable mechanical stirring at a moderate speed of spin at 40 °C for about two hours with continuous stirring in order to form a homogeneous solution and also to be sure that CA was completely dissolved. The blended solutions were casted carefully on glass plates and placed onto a table waiting for about two hours in air to get rid of any air bubbles. casting solution was then put in a dryer at 60 °C for about three days so as to be dried. Then the dried samples were carefully taken off from the glass plates using sharp knife. The structure characterization of the blend materials was investigated by X-ray diffraction (XRD). XRD spectra was obtained using A Philips X-ray diffractometer (model Philips X'Pert) worked at 40 kV and 25 mA was used in the measurements with utilized the monochromatic CuK α ($\lambda=1.5408 \text{ \AA}$). The transmittance, T, and the reflectance, R, of the blend materials were measured at normal incidence in the spectral range 300–1400 nm using a double-beam spectrophotometer (JASCO, V-570 UV-Vis-NIR).

3 Result and discussion

3.1 X-ray diffraction (XRD) analysis

XRD was utilized to estimate the peak broadening with crystallite size (Yogamalar et al. 2009). The XRD patterns of the prepared samples of pure CA and CA blended with different concentration of MoO₃-NPs are represented in Figure 1. As presented in the figure, there were two amorphous humps centered at $2\Theta=12^\circ$ and 18° for pure cellulose acetate which were in good agreement with (Moraes et al. 2015; Samsi et al. 2016). Due to blending with 0.25 wt% of MoO₃-NPs, three peaks were observed at $2\Theta=11^\circ$, 14° and 17° corresponding to the reflection from the plane (100), (110) and (200) respectively. However, increasing the concentrations of MoO₃-NPs to 0.5 wt%, two characteristic peaks were observed at $2\Theta=26^\circ$ and 39° which corresponding to (210) and (224), respectively. Additionally, the intensities of the peaks observed at 0.5% wt%, were increased upon increasing the concentration of MoO₃-NPs up to 1% wt%. These peaks indicate the presence of MoO₃-NPs with its hexagonal structure correspond to that of JCPDS Card no. 21-0569. Moreover, it was observed that there was a decrease in the hump intensity centered at $2\Theta=12^\circ$ with increasing the concentration of MoO₃-NPs which may indicate that the sample exhibit partially crystallizes upon adding MoO₃-NPs.

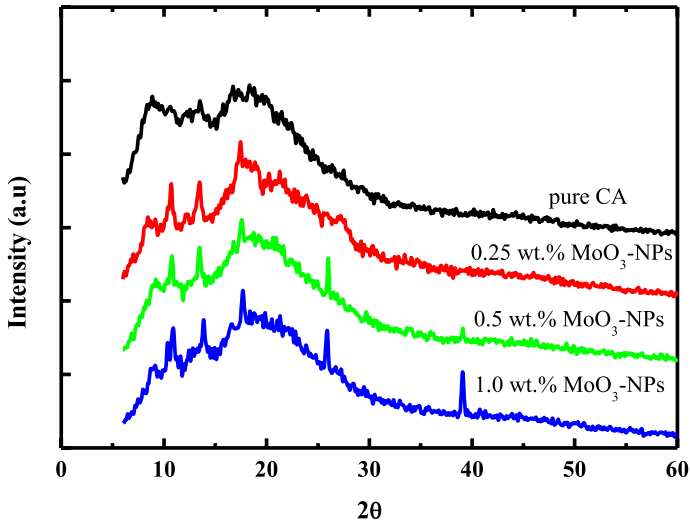


Fig. 1 XRD of pure CA and CA blended with different concentration of MoO_3

3.1.1 The crystallite size and strain evaluations using Size–Strain plot (SSP) method

Crystallite size can be considered as a measure of size of coherently diffracting domains. It is not generally like the particle size because of the formation of polycrystalline aggregates (Ramakanth 2007; Zhang et al. 2006). Lattice strain can be considered as a measure of the distribution of lattice constants resulting from crystal imperfections, such as lattice dislocations, the grain boundary triple junction, contact or sinter stresses, stacking faults and coherency stresses (Alghunaim et al 2017). Crystallite size as well as lattice strain affect the Bragg peak in varying methods. They both increase the peak width and intensity and as a result, shift the 2θ peak position. The effect of other uniform strain or nonuniform. SSP method is considered for the crystal structure isotropic nature. It is supposed that Lorentzian profile describe crystallite size profile and Gaussian function that describe strain profile (Zak et al. 2011; Tagliente and Massaro 2008), then we get the equation:

$$(d\beta \cos \theta)^2 = \frac{k}{D} (d^2 \beta \cos \theta)^2 + (\varepsilon/2)^2 \quad (1)$$

The term $(d\beta \cos \theta)^2$ is plotted against $(d^2 \beta \cos \theta)$ as represented in Fig. 2. The particle size and strain are determined from the slope and interception of the linearly fitted data. It appears from the results of the SSP model was accurate method or determination of MoO_3 -NPs as the data were fitted in a precise way as all data points touching fitting line. And so, the crystallite size getting from the data is tabulated in Table 1. As observed from the table the particle size as well as the strain were increased with increasing MoO_3 concentration.

The lattice parameters, including the lattice constants (a and c) and cell volume (v_{Cell}), for hexagonal structure were calculated according to the following (Shahroz et al. 2022a, b, c; Shahroz et al. 2023; Jameel et al. 2023; Numan et al. 2023):

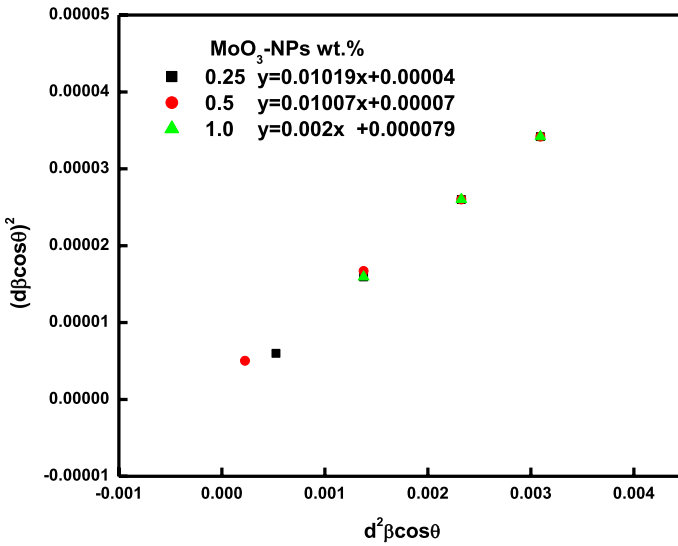


Fig. 2 The SSP plot for CA with 1wt% concentration of MoO₃. The particle size is achieved from the slop of the liner fitted data

Table 1 The crystallite size, strain and lattice parameters for blended sammples with different concentration of MoO₃-NPs

MoO ₃ -NPs wt%	Dnm	ε	d-spacing A°	Lattice constant (a) A°	Lattice constant (c) A°	Lattice Volume A° ³
.25	92.25	0.013	3.45	8.9	12.7	1006
0.50	93.3	0.016	4.56	10.5	15	1653.8
1.00	94	0.018	5.29	10.6	15.14	1701.1

$$\frac{1}{d^2} = \frac{4}{3} \left(\frac{h^2 + hk + k^2}{\alpha^2} \right) + \frac{l^2}{c^2} \tag{2}$$

$$V_{cell} = a^2c \tag{3}$$

The lattice parameters for the blended sample are tabulated in Table 1. It was observed that the particle size as well as the lattice parameter increase with increasing the concentration of MoO₃-NPs and hence the cell volume also increase. This increase may be due to the formation of hydrogen bond between MoO₃-NPs and CA which in role increasing the strain due to increase in the electrostatic force (Harumi et al. 2006).

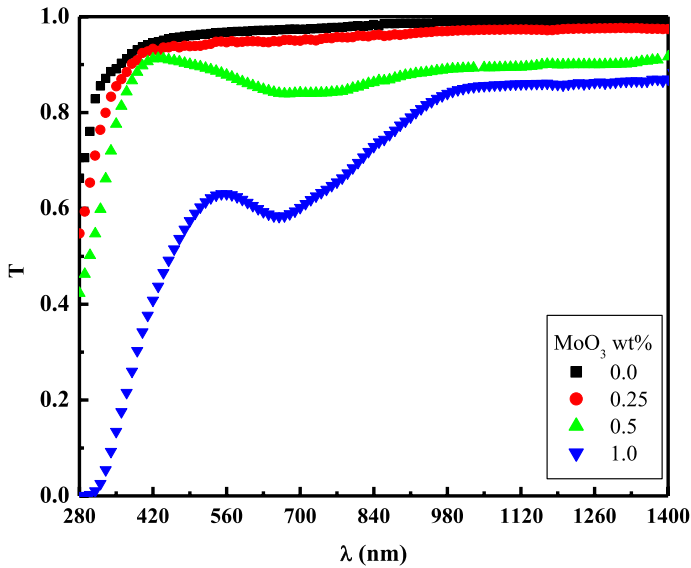


Fig. 3 The optical transmittance $T(\lambda)$ for pure CA and CA with different concentration of MoO_3

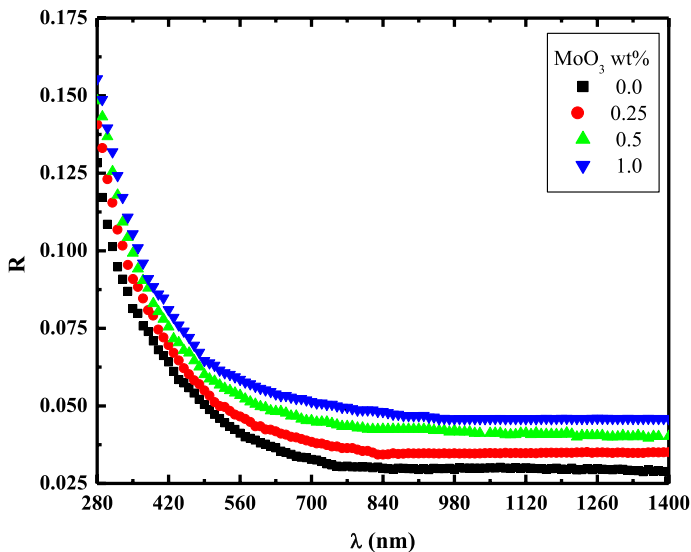


Fig. 4 The optical reflectance $R(\lambda)$ for pure CA and CA with different concentration of MoO_3

4 Optical studies

The spectral behavior of the transmittance, $T(\lambda)$, and the reflectance, $R(\lambda)$ for pure CA and CA blended with different concentrations of MoO_3 -NPs in wavelength range (300–1300) nm are shown in Figs. 3 and 4. It was observed that the pure CA film

shows high transparency about 1 in comparison with the blended films this result in agreement with Radhika et al. (2017). The transparency was observed to decline with increasing MoO₃ loading. This large decrease in optical transmittance can be useful to use in window applications (Zakir et al. 2021). An edge was observed to form in visible region in wavelength range (370–450) nm upon adding the concentration of 0.5 wt% of MoO₃-NPs. This edge was observed to shift to higher wavelength in the wavelength range (500–550) nm (red shift) upon increasing the concentration of MoO₃ to 1 wt%. This edge may be attributed to the electron excitation from the HOMO band to the LUMO band (El-Nahass and Desoky 2017). The absorption region separated from the transmission region by that optical transmission edge. Filter material can be a good application recommended for the blended material to use because of the presence of such edge (Darwish et al. 2016). The Reflectance as shown in Fig. 4 was observed to increase with increasing MoO₃-NPs loading which may be due to the formation of intermolecular hydrogen bonding between MoO₃-NPs and cellulose acetate and thus the cellulose acetate films become denser, so lower transmittance and higher reflectance can be achieved (Abdullah et al. 2016).

The spectral values of R and T at different wavelengths Taken in consideration in order to evaluate the absorption coefficient, α and the refractive index, n by using the following equations (Zeyada et al. 2010):

$$\alpha = \frac{1}{d} \ln \left[\frac{(1 - R^2)/2T + \sqrt{((1 - R)^4/4T^2) + R^2}}{1} \right] \quad (4)$$

$$\kappa = \alpha \lambda / 4\pi \quad (5)$$

$$n = ((1 + R)/(1 - R)) + \sqrt{(4R/((1 - R)^2) - \kappa^2)} \quad (6)$$

as d represent the sample thickness and κ is the extinction coefficient.

Figure 5 represents the absorption coefficient, $\alpha(h\nu)$ for pure CA and CA blended with different concentrations of MoO₃-NPs. The figure showed a slightly increase in the calculated value of α with increasing the MoO₃-NPs concentration. There was observed an absorbance edge in the sample with concentration of 0.5 wt% that was observed to shift to lower energy with increasing MoO₃-NPs concentration. The edge may be caused as a result of charge transportation from the valence band made up of 2p orbitals of oxygen anions (O²⁻) in MoO₃-Nps to the conduction band made up of 3d orbitals of Mo cations with increasing MoO₃-NPs concentration due to the increase in the interatomic interaction. The red-shift in absorption edges can be explained by this interpretation which indicate the decrease in the optical energy gap of the material with increasing the concentration of MoO₃-NPs (Radhika et al. 2017; Yuan et al. 2017).

The absorption of light by non-solid molecular media is described by the molar extinction coefficient ϵ_{molar} which can be obtained from using absorption coefficient by the following equation (Zeyada et al. 2010):

$$\epsilon_{\text{molar}} = (\alpha/2.303) (M/\rho) \quad (7)$$

where M and ρ is the molecular weight and solid mass density respectively. The Spectral distribution of the molar extinction coefficient ϵ_{molar} for CA film and CA blended with different concentration of MoO₃-NPs was demonstrated in Fig. 6. The electric dipole strength

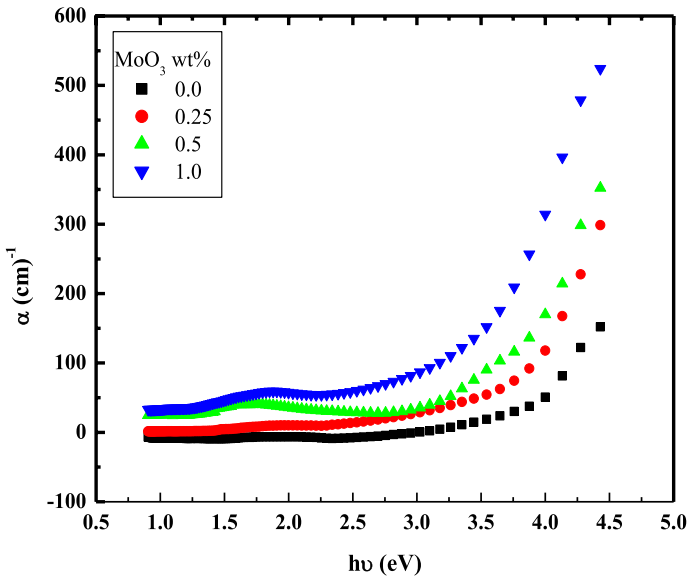


Fig. 5 The optical absorbance $\alpha(h\nu)$ for pure CA and CA with different concentration of $\text{MoO}_3\text{-NPs}$

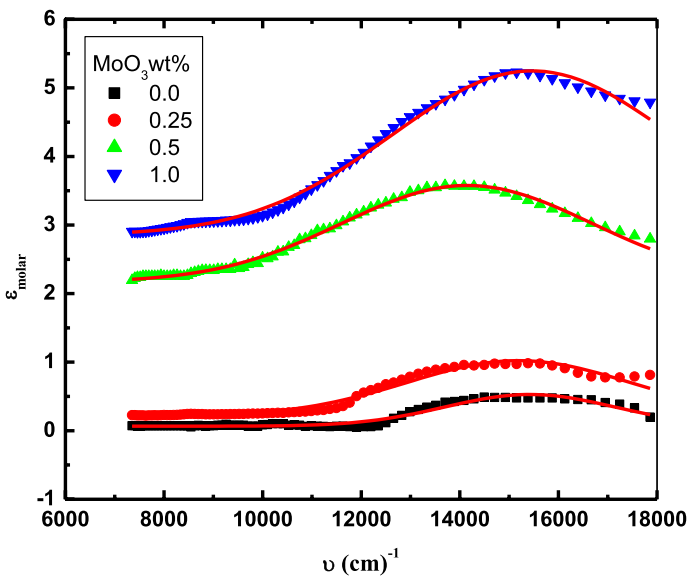


Fig. 6 Molar extinction coefficient spectra $\epsilon_{\text{molar}}(\nu)$ of pure CA and CA with different concentration of $\text{MoO}_3\text{-NPs}$

q^2 and the oscillator strength, f , can be calculated by making a Gaussian profile to the peak exist in the spectra according to equations:

$$q^2 = (1/2500)\epsilon_{\text{molar}}(\Delta\lambda/\Delta\lambda_{\text{max}}) \tag{8}$$

$$f = 4.3 \times 10^{-9} \int \epsilon_{molar} \nu d\nu \quad (9)$$

where $\Delta\lambda$ is the absorption half band width, ν is the wavenumber and λ_{max} is the wavelength at maximum absorption. Gaussian profile for all studied samples is shown with red line in Fig. 6. The values of f and q^2 calculated for the peak appeared for CA and CA with different concentration of MoO₃-NPs are listed in Table 2.

The type of the transition and the value of optical energy gap can be estimated using the absorption coefficient by the well-known Tauc relation (Bardeen] et al. 1965):

$$(\alpha h\nu) = B (h\nu - E_g)^r \quad (10)$$

where B is a constant and r is constant evaluate the nature of band transition where r is equal to $1/2$ in direct allowed transition, $2/3$ in direct forbidden transition, 2 in indirect allowed transition and equal to 3 in indirect forbidden transition. It was found that by differentiate Eq. (8) with respect to $h\nu$:

$$(d(\alpha h\nu)/d(h\nu)) = Br (h\nu - E_g)^{r-1} \quad (11)$$

Dividing Eq. (8) by the product of the differentiation Eq. (9):

$$\alpha h\nu / (d(\alpha h\nu)/d(h\nu)) = 1/r(h\nu - E_g) \quad (12)$$

So type and value of the transition can be evaluated (Zeyada et al. 2012):

Figure 7 illustrates the variation $\alpha h\nu / (d(\alpha h\nu)/d(h\nu))$ versus $h\nu$ for CA with different concentration of MoO₃-NPs. The figure shows a straight line whose reciprocal of its slope calculate the type of electronic transition. The energy gap E_g values was determined by extrapolation the straight line to intercept. The best fitting of results showed that the indirect allowed transition are responsible for the interband transition of CA with different concentration of MoO₃-NPs, and the HOMO–LUMO energy gaps are 3.23, 3.15, 3 and 2.86 eV for CA with different concentration of MoO₃-NPs, respectively. The plot of $(\alpha h\nu)^{1/2}$ against $h\nu$ for CA with different concentration of MoO₃-NPs shown in Fig. 8. By extrapolation of the straight line part of the curve $(\alpha h\nu)^{1/r} = 0$, the value of indirect optical energy gap was gotten. The values of energy gaps for films are listed in Table 3. Two optical indirect allowed transitions are observed for all samples as shown in the figure. The low energy transition is corresponding to onset gap which may be due to $n-\pi^*$ transition. The second transition due to $\pi-\pi^*$ transition corresponding to HUMO-LOMO gap (Soret band) whose value was found to be 3.23 eV for pure cellulose acetate and this result is in a good agreement with Necula et al. (2010). It was observed that the values of onset gaps and the HOMO–LUMO gap decrease with increasing the concentration of MoO₃-NPs which is shown in Fig. 9 (Dangi et al. 2022).

Table 2 The electric dipole strength q^2 and oscillator strength f for CA with different concentration of MoO₃-NPs

MoO ₃ -NPs wt%	q^2 (nm) ²	f
0.00	0.2	8.5E–6
0.25	0.5	2.0E–5
0.50	2.0	3.9E–5
1.00	2.3	7.4E–5

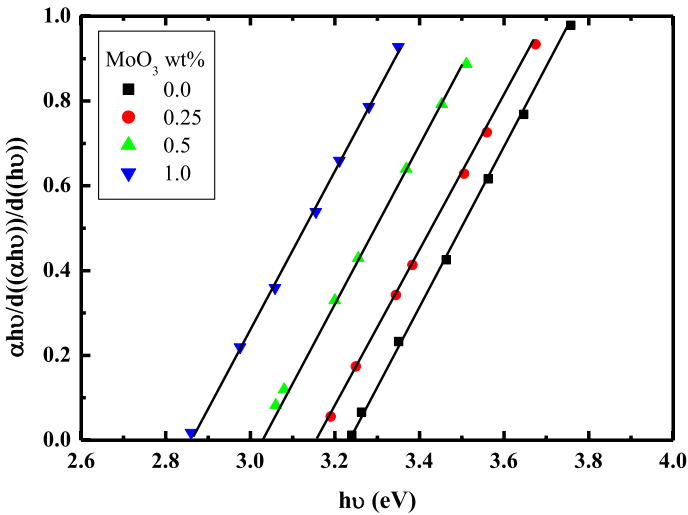


Fig. 7 Variation in $[\alpha h\nu / d((\alpha h\nu) / d(h\nu))]$ versus $h\nu$ for CA with different concentration of MoO_3

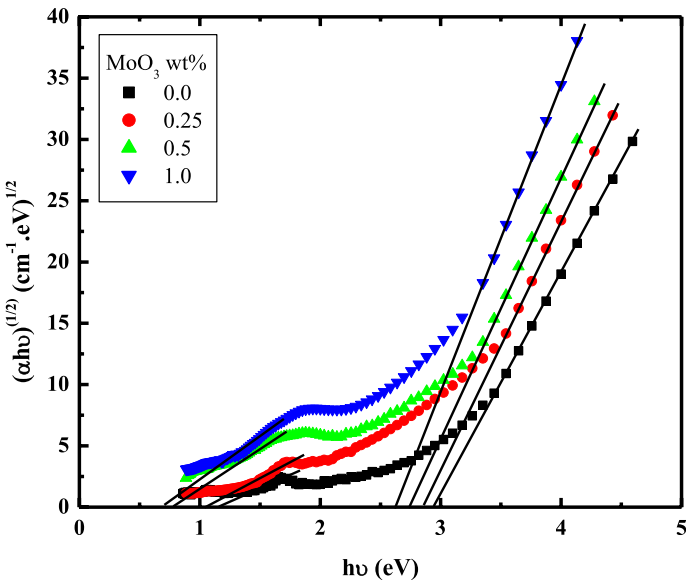
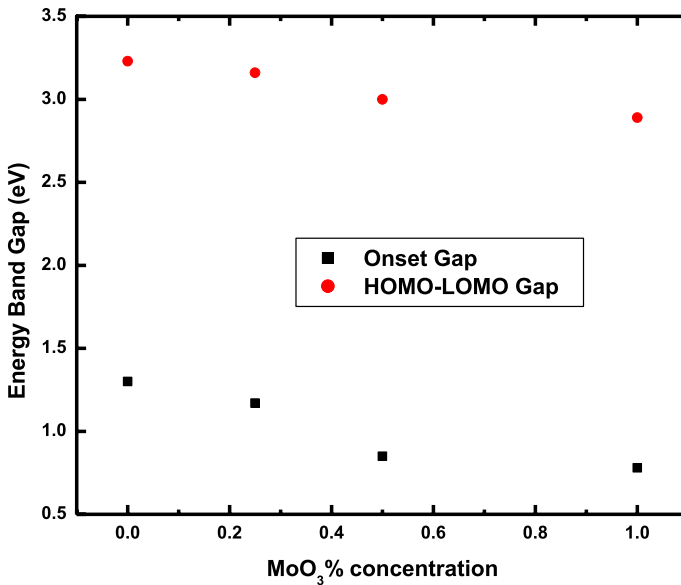


Fig. 8 Variation of $(\alpha h\nu)^{1/2}$ as a function of photon energy ($h\nu$) for pure CA and CA blended with varying concentration of MoO_3

Density of state model suggested by Mott and Davis can explain this decrease in optical band gap of material (Mott and Davis 1979). The optical absorption in the pure amorphous sample depends on short-range order and on the existing defects. The model suggested that the localized states width of the near the mobility edges is controlled by the degree of disorder and defects present in the amorphous material. Also the decrease in optical band gap of the material come from the existence of high concentration of

Table 3 Optical parameter of pure CA and CA with different concentration of MoO₃

Wt% MoO ₃	Absorption parameter		Dispersion parameter				
	Onset gab (eV)	HOMO–LUMO gab (eV)	E _O (eV)	E _d (eV)	ε _∞	ε _l	N/M* (g ⁻¹ cm ⁻³)
0	1.3	3.23	7	6.8	1.97	2.43	2.95 × 10 ⁴⁶
0.25	1.17	3.16	6.54	6.95	2.06	2.5	1.96 × 10 ⁴⁶
0.50	0.85	3.00	6.14	7.4	2.2	2.7	1.47 × 10 ⁴⁶
1.00	0.78	2.89	6.09	7.81	2.28	2.83	9.82 × 10 ⁴⁵

**Fig. 9** Variation of energy band gap as a function of MoO₃-NPs wt%concentration

localized states in the band structure. The model suggested also that the reduction can be a result of the shift in Fermi level whose position is determined after the distribution of electrons over the localized states due to the addition of MoO₃-NPs (Ghanipour and Dorrnian 2013).

The spectral distribution of refractive index (n) for CA films with different concentration of MoO₃-NPs was shown in Fig. 10. The value of refractive index is in agreement with that of Adina Maria Necula et al. (Mott and Davis 1979). It is clearly observed that the refractive index exhibited an anomalous dispersion for $\lambda < 460$ nm and normal dispersion for $\lambda > 460$ nm. The values of refractive index were observed to increase with increasing the concentration of MoO₃ which the same trend as the reflectance (Abdullah et al. 2016).

Normal dispersion behavior of n for cellulose acetate films can be further explained using the model of the free single oscillator that is expressed by Wemple-DiDomenico (1971; Wemple et al. 1973) as follows:

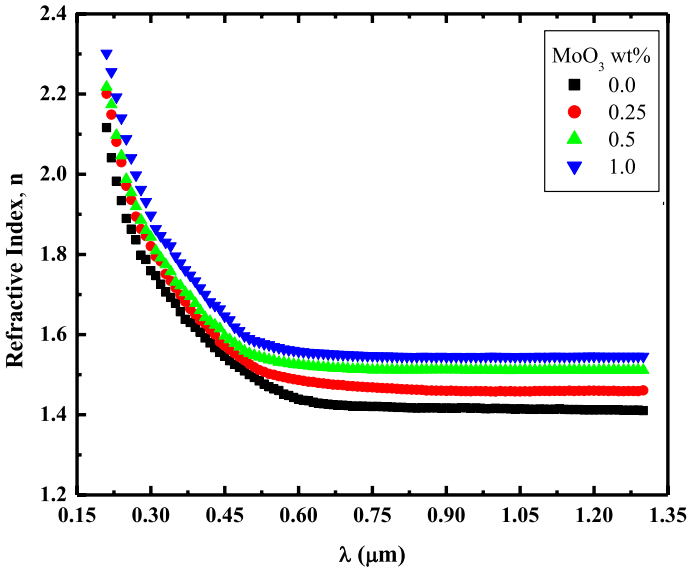


Fig. 10 Variation of refractive index n as a function of photon energy ($h\nu$) for pure CA and CA blended with varying concentration of MoO_3

$$n^2(h\nu) - 1 = E_o E_d / (E_o^2 - (h\nu)^2) \tag{13}$$

The single oscillator energy E_o stimulates all electronic excitations involved as well as E_d is the dispersion energy, which is pertaining to the optical transition average oscillator strength. Figure 11 shows the plot of $(n^2 - 1)^{-1}$ versus $(h\nu)^2$ for the films. From the slope and intercept of the linear parts in the graph, E_o and E_d values are determined and listed in

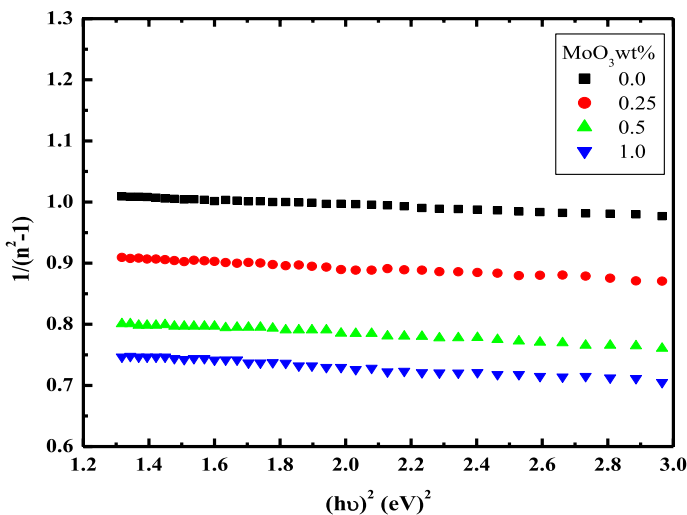


Fig. 11 The relation between $(n^2 - 1)^{-1}$ and $(h\nu)^2$ for CA with different concentration of MoO_3

Table 3. E_0 was observed to decrease with increasing the concentration of MoO_3 . This may be due to the low energy transition which improved by the increasing of localized states in the energy gap (Ghanipour and Dorrani 2013). The dispersion energy E_d was observed to increase with increasing the concentration of MoO_3 . It was found that the oscillation energy is approximately twice HOMO-LUMO gap for the samples, this result achieved the relation that was given by Tanaka (1980).

The infinite high frequency dielectric constant ϵ_∞ is calculated from the dispersion relation by extrapolating the linear segment of the relation between $(n^2 - 1)^{-1}$ and square of photon energy, $(h\nu)^2$. The value of infinite high frequency dielectric constant ϵ_∞ was observed to increase with increasing the concentration of MoO_3 -NPs.

The real component of dielectric constant ϵ is related to λ^2 , by the following relation:

$$n^2 = \epsilon_l - \left(\frac{e^2 N}{4\pi^2 \epsilon_0 m^* c^2} \right) \lambda^2 \quad (14)$$

where ϵ_l , is the empty lattice dielectric constant, e is the elementary charge, ϵ_0 is the permittivity of free space and N/m^* can be defined to be the ratio of free carrier concentration to the free carrier effective mass.

A linear relation between n^2 and λ^2 is represented in Fig. 12. The value of the ratio N/m^* and ϵ_l are calculated from the slope and interception of the straight line respectively. The values of ϵ_l and (N/m^*) are listed also in Table 3. The table represents that the value of ϵ_l is larger than that of high frequency dielectric constant ϵ_∞ which indicate the contribution of free charge carriers to the infinite dielectric constant. Table 3 also shows that the value of (N/m^*) ratio is too high which attributed to the small electron effective mass (El-Nahass et al. 2010).

The real, ϵ_1 , and imaginary, ϵ_2 , parts of the complex dielectric constant and the loss tangent, $\tan \delta$ can be calculated according to the following relations (Muhammad et al. 2021):

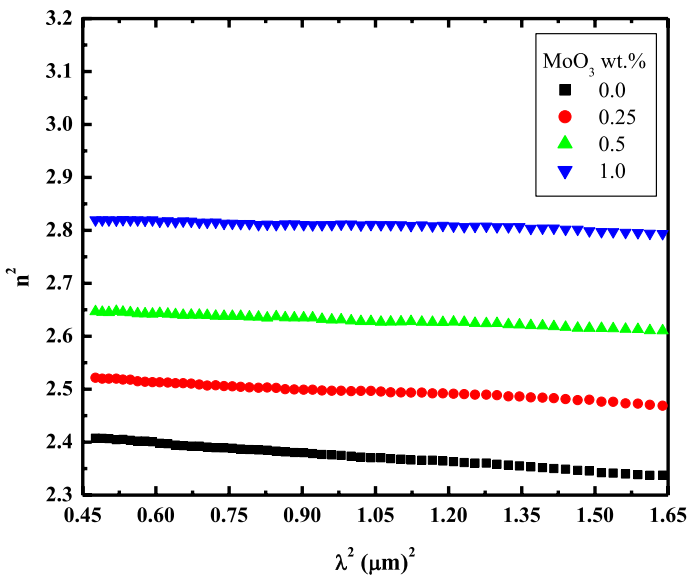


Fig. 12 The relation between n^2 and $(h\nu)^2$ for CA with different concentration of MoO_3

$$\varepsilon_1 = n^2 - k^2 \quad (15)$$

$$\varepsilon_2 = 2nk \quad (16)$$

$$\tan \delta = \varepsilon_2 / \varepsilon_1 \quad (17)$$

where n and k are refractive and absorption indices respectively and $\tan \delta$ is the phase difference between the applied electric field and the induced current. ε_1 determines the maximum material storage for energy. ε_2 , also called the relative loss factor, display the dielectric material absorption of electrical energy that is exposed to an alternating electromagnetic field. The loss tangent describes the material absorption extent of electromagnetic field (El-Nahass et al. 2012).

Figures 13 and 14 represent the variation of ε_1 , ε_2 with photon energy for CA and CA with different concentration of MoO₃-NPs. It was observed that the variation of ε_1 follows the same trend as n , with wavelength as well as the variation of ε_2 also follows the behavior of variation of α , with photon energy. The variation of $\tan \delta$ for CA and CA with different concentration of MoO₃-NPs as a function of photon energy are shown in Fig. 15. The behavior of ε_1 , ε_2 with photon energy for CA and CA with different concentration of MoO₃-NPs is observed to be similar to that of dielectric constant and dielectric loss at high frequency in our previous work (Ezzat et al. 2021).

The damping constant γ_o can be calculating according to Eq. (15) from the slope of the fitting of the straight line of relation between λ^3 vs $\varepsilon_{\text{molar}}$ as shown in Fig. 16.

$$\varepsilon_2 = 2nk = \frac{q^2 N}{8\pi^2 \varepsilon_0 m * c^3} \gamma_o \lambda^3 \quad (18)$$

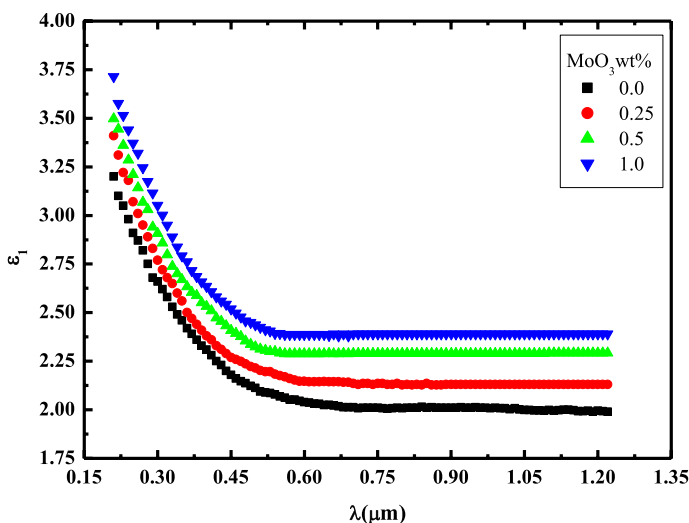


Fig. 13 The relation between ε_1 and λ for CA with different concentration of MoO₃-NPs

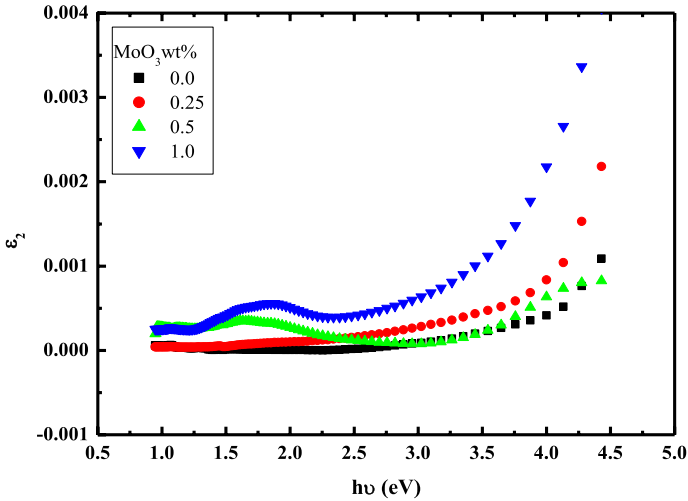


Fig. 14 The relation between ε_2 and $h\nu$ for CA with different concentration of MoO_3 -NPs

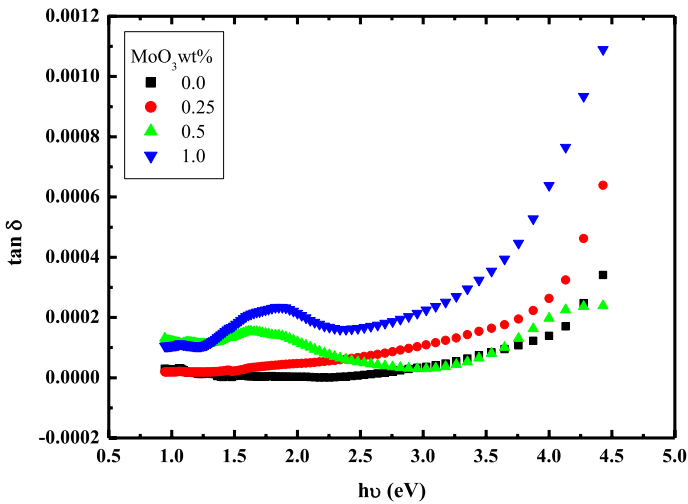


Fig. 15 The relation between $\tan \delta$ and $h\nu$ for CA with different concentration of MoO_3 -NPs

Values of damping constant γ_o for cellulose acetate with different concentration of MoO_3 -NPs are shown in Table 4.

It was observed the presence of Urbach tail which obeys the empirical relation:

$$\alpha = \alpha_o \exp\left(\frac{h\nu}{E_u}\right) \quad (19)$$

where, α_o , is a constant depend on the characteristics of the polymers and E_u is Urbach energy, which measures the degree of disorder within the material.

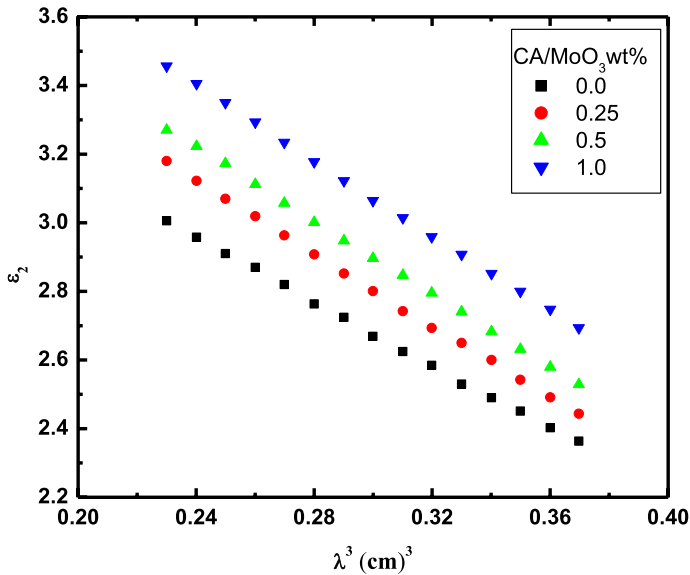


Fig. 16 The relation between ϵ_2 and λ^3 for CA with different concentration of MoO_3 -NPs

Table 4 Values for damping oscillation for CA with different concentration of MoO_3 -NPs

MoO_3 -NPs wt%	$\gamma_o \text{ cm}^{-1}$
0	1.02E+05
0.25	1.74E+05
0.5	2.35E+05
1.0	3.61E+04

The value of Urbach energy E_u is determined according to the equation from the reciprocal of the slope of the straight line from the relation between $h\nu$ and $\ln \alpha$ as shown in Fig. 17. It was observed that Urbach energy values increases with increasing MoO_3 -NPs concentration; this was shown in the inset which can be attributed to the creation of localized states at the band gap as a result of the addition of MoO_3 which can increase the disorder in the material. The increase in point defect concentration is resulted from this disorder which resulted in a large number of possible bands to tail and tail to tail transitions (Abdel-Rahim et al. 2014).

5 Conclusions

Casting method was used to prepare CA and CA/ MoO_3 -NPs with MoO_3 -NPs concentrations of 0.25 wt%, 0.5 wt% and 1.0 wt%. XRD results indicate the amorphous nature of pure CA film. The addition of MoO_3 resulted in partially crystallize of the sample. Size–Strain plot (SSP) method calculation was used to analyze X-ray data for the blended samples and to calculate the particle size. The particle size was observed to increase with increasing MoO_3 concentration. Tauc's equation was used for the analysis

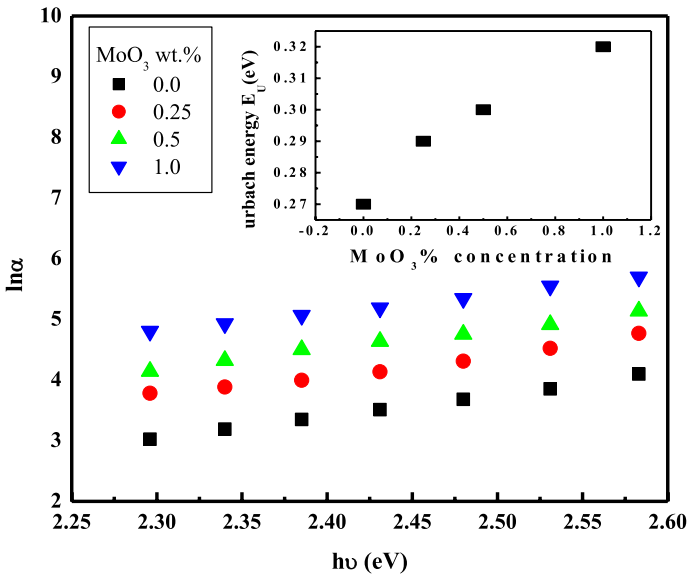


Fig. 17 Plotting of $\ln\alpha$ as a function of photon energy ($h\nu$) for CA with different concentration of MoO_3

of optical transitions occurring in (CA) and CA/ MoO_3 -NPs. The optical transitions in the films are indirect in nature. There were observed two energy gaps which corresponding to HOMO–LUMO gap and Onset gap. A gradual red shift is observed in the energy band gap values with increasing MoO_3 -NPs concentration from 3.23 eV pure film to 2.89 eV for blended film in HOMO–LUMO gap and from 1.3 eV pure film to 0.87 eV for blended film for onset gap. This decrease can mainly be attributed to the increases of concentration of the localized states in the band structure with increasing the concentration of MoO_3 . Classical single-oscillator model was used to analyze normal region of the refractive dispersion. Using the single-oscillator model, we have found that the oscillator energy (E_o) is found to decrease with increasing the concentration of MoO_3 from 7 to 6.09 eV and the dispersion energy (E_d) is found to increase from 6.8 eV for pure film to 7.81 eV after blended with MoO_3 . There observed a difference between the values of ϵ_∞ and ϵ_l which may be due to contribution of the free carrier concentration. Urbach energy was calculated and was observed to increases with increasing MoO_3 -NPs concentration. Molar extinction coefficient was calculated for studied sample. From Gaussian profile electric dipole strength, q^2 , and the oscillator strength, f , are calculated. The spectral distribution of real and imaginary part of dielectric constant and loss factor are studied. The maximum energy storage of material (real part of dielectric constant ϵ_1) was observed to increase with increasing MoO_3 -NPs which make the material promising for energy storage applications. Damping frequency was calculated from the slope of relation between λ_3 and ϵ_2 .

Author contributions Dina ezzat and mahmoud El-Nahas prepared figurehanan and Mortada wrote the main manuscript text

Funding Open access funding provided by The Science, Technology & Innovation Funding Authority (STDF) in cooperation with The Egyptian Knowledge Bank (EKB). The authors have not disclosed any funding.

Declarations

Competing interests The authors declare no competing interests.

Open Access This article is licensed under a Creative Commons Attribution 4.0 International License, which permits use, sharing, adaptation, distribution and reproduction in any medium or format, as long as you give appropriate credit to the original author(s) and the source, provide a link to the Creative Commons licence, and indicate if changes were made. The images or other third party material in this article are included in the article's Creative Commons licence, unless indicated otherwise in a credit line to the material. If material is not included in the article's Creative Commons licence and your intended use is not permitted by statutory regulation or exceeds the permitted use, you will need to obtain permission directly from the copyright holder. To view a copy of this licence, visit <http://creativecommons.org/licenses/by/4.0/>.

References

- Azelia, W.C., Rajkumar, B., Chan-Woo, P., Ji-Soo, P., Eun-Ah, L., Jeong-Ki, K., Song-Yi, H., Seung-Hwan, L.: Preparation and characterization of cellulose acetate film reinforced with cellulose nanofibril. *Polymers* **13**(17), 2990–3007 (2021)
- Abdullah, O.G., Aziz, S.B., Rasheed, M.A.: Structural and optical characterization of PVA: KMnO_4 based solid polymer electrolyte. *Results Phys.* **6**, 1103–1108 (2016)
- Abdel-Rahim, M.A., Abdel-Latif, A.Y., Rashad, M., Abdelazim, N.M.: Annealing effect on structural and optical properties of $\text{Se}_{87.5}\text{Te}_{10}\text{Sn}_{2.5}$ thin films. *Mater. Sci. Semicond. Process.* **20**, 27–34 (2014)
- Căprărescu, S., Zgârian, R.G., Tihan, G.T., Purcar, V., Totu, E.E., Modrojan, C., Chiriac, A.L., Nicolae, C.A.: Biopolymeric membrane enriched with chitosan and silver for metallic ions removal. *Polymers* **12**, 1792–1814 (2020)
- Archana, M.D., Abdul, A.A., Manash, P.H.: Synthesis and characterization of cellulose acetate from rice husk: Eco-friendly condition. *Carbohydr. Polym.* **112**, 342–349 (2014)
- Alghunaim, N.S., Omar, A.Y., Elhaes, H., Ibrahim, M.A.: Effect of ZnO and TiO_2 on the reactivity of some polymers. *J. Comput. Theor. Nanosci.* **4**(8), 2838–2843 (2017)
- Badry, R., El-Kohdary, S., Elhaes, H., Nada, N.A., Ibrahim, M.A.: The influence of moisture on the electronic properties of monomer, dimer, trimer and emeraldine base sodium carboxymethyl cellulose. *Egypt. J. Chem.* **7**, 39–56 (2019)
- Baeg, K.J., Caironi, M., Noh, Y.Y.: Toward printed integrated circuits based on unipolar or ambipolar polymer semiconductors. *J. Adv. Mater.* **25**, 4210–4244 (2013)
- Bardeen, J., Slatt, F.J., Hall, L.: Photoconductivity Conference. Wiley, New York (1965)
- Chabba, S., Matthews, G.F., Netravali, A.N.: 'Green' composites using cross-linked soy flour and flax yarns. *Green Chem.* **7**, 576–581 (2005)
- Chen, Y.J., Gao, X.M., Di, X.P., Ouyang, Q.Y., Gao, P., Qi, L.H., Li, C.Y., Zhu, C.L.: Porous iron molybdate nanorods: in situ diffusion synthesis and low-temperature H_2S gas sensing. *ACS Appl. Mater. Interfaces* **5**, 3267–3274 (2013)
- Darwish, A.A., Abu-Samah, F.S.A., Mohamed, Z., El-Nahass, M.M.: Influence of film thickness and annealing temperature on optical properties of nanostructured- TiO_2 thin films prepared by sol-gel spin coating technique. *Int. J. Nanosci.* **15**, 1650028–1650029 (2016)
- Dangi, S.B., Hashmi, S.Z., Upendra, K., Choudhary, B.L., Kuznetsov, A.E., Saurabh, D., Shalendra, K., Dolia, S.N., Sudhish, K., Balsam, F.I.S., Reem, D., Hasan, P.M.Z., Alvi, P.A.: Exploration of spectroscopic, surface morphological, structural, electrical, optical and mechanical properties of biocompatible PVA-GO PNCs. *Diam. Relat. Mater.* **127**, 109158–109178 (2022)
- El-Nahass, M.M., Desoky, W.M.: Investigating the structural and optical properties of thermally evaporated 1,3,3-trimethylindolino-b-naphthopyrylospiran thin films. *Appl. Phys. A* **123**, 517–533 (2017)
- El-Nahass, M.M., El-Deeb, A.F., Metwally, H.S., Hassanien, A.M.: Structural and optical properties of iron (III) chloride tetraphenylporphyrin thin films. *Eur. Phys. J. Appl. Phys.* **52**, 10403–10409 (2010)

- El-Nahass, M.M., Ali, M.H., El-Denglawey, A.: Structural and optical properties of nano-spin coated sol-gel porous TiO₂ films. *Trans. Nonferrous Met. Soc. China* **22**, 3003–3011 (2012)
- Ezzat, D., Youssif, M., Elhaes, H., El-Nahass, M.M.: Dielectric relaxation behaviour and AC electrical conductivity of cellulose acetate-molybdenum trioxide nanoparticle blended film, *Egypt. J. Chem.* **64**(3), 1125–1132 (2021)
- Ezzat, H.A., Menazea, A.A., Omara, W., Basyouni, O.H., Helmy, S.A., Mohamed, A.A., Tawfik, W., Ibrahim, M.A.: DFT:B3LYP/ LANL2DZ study for the removal of Fe, Ni, Cu, As, Cd and Pb with Chitosan. *Biointerface Res. Appl. Chem.* **10**(6), 7002–7010 (2020)
- Ezzat, H.A., Maroof, A.H., Nada, A.N.A., Ibrahim, M.A.: Effect of nano metal oxides on the electronic properties of cellulose, Chitosan and sodium alginate. *Biointerface Res. Appl. Chem.* **8**(4), 4143–4149 (2019)
- Ezzat, D., Mahmoud, A.A., El-Nahass, M.M., Elhaes, H.: Effect of ZnO concentration upon the structural properties of cellulose acetate. *J. Middle East Appl. Sci. Technol.* **5**, 64–72 (2015)
- Fakhri, A., Nejad, P.A.: Antimicrobial, antioxidant and cytotoxic effect of molybdenum trioxide nanoparticles and application of this for degradation of ketamine under different light illumination. *J. Photochem. Photobiol. b* **159**, 211–217 (2016)
- Frederik, C.K.: Fabrication and processing of polymer solar cells: a review of printing and coating techniques. *Sol. Energy Mater. Sol. Cells* **93**, 394–412 (2009)
- Ghanipour, M., Dorrani, D.: Effect of Ag-nanoparticles doped in polyvinyl alcohol on the structural and optical properties of PVA films. *J. Nanomater.* **2013**, 897043–897110 (2013)
- Harumi, S., Rumi, M., Jianming, Z., Yukihito, O., Katsuhito, M., Isao, T., Hikaru, T., Isao, N.: X-ray diffraction and infrared spectroscopy studies on crystal and lamellar structure and CHO hydrogen bonding of biodegradable Poly(hydroxyalkanoate). *Macromol. Res.* **14**(4), 408–415 (2006)
- Hashmi, S.Z., Upendra, K., Choudhary, B.L., Kuznetsov, A.E., Saurabh, D., Shalendra, K., Savas, K., Dolia, S.N., Alvi, P.A., Vimala, D.: Spectroscopic studies, molecular structure optimization and investigation of structural and electrical properties of novel and biodegradable Chitosan-GO polymer nanocomposites. *J. Mater. Sci.* **55**, 14829–14847 (2020)
- Ibrahim, M.A., Osman, O., Mahmoud, A.A.: Spectroscopic analyses of cellulose and chitosan: FTIR and modeling approach. *J. Comput. Theor. Nanosci.* **8**, 117–123 (2011)
- Jameel, M.H., Roslan, M.S.B., Mayzan, M.Z.H.B., Shaaban, I.A., Rizvi, S.Z.H., Agam, M.A.B., Saleem, S., Assiri, M.A.: A comparative DFT study of bandgap engineering and tuning of structural, electronic, and optical properties of 2D WS₂, PtS₂, and MoS₂ between WSe₂, PtSe₂, and MoSe₂ materials for photocatalytic and solar cell applications. *J. Inorg. Organomet. Polym.* **33**, 821–835 (2023)
- Li, C., Adamcik, J., Mezzena, R.: Biodegradable nanocomposites of amyloid fibrils and graphene with shapememory and enzyme-sensing properties. *Nat. Nanotechnol.* **7**, 421–427 (2012)
- Michalet, X., Pinaud, F.F., Bentolila, L.A., Tsay, J.M., Doose, S., Li, J.J., Sundaresan, G., Wu, A.M., Gambhir, S.S., Weiss, S.: Quantum dots for live cells, in vivo imaging, and diagnostics. *Science* **307**, 538–544 (2005)
- Mochalin, V.N., Gogotsi, Y.: Wet chemistry route to hydrophobic blue fluorescent nanodiamond. *J. Am. Chem. Soc.* **131**, 4594–4595 (2009)
- Muhammad, H.J., Shahroz, S., Muhammad, H., Muhammad, S.R., Hamoud, H.N.S., Mahmoud, M.H., Zeinhom, M.E., Muhammad, G.B.A., Maytham, Q.H., Abdullah, H.J., Jibrin, A.Y., Mohd, A.B.A.: A comparative study on characterizations and synthesis of pure lead sulfide (PbS) and Ag-doped PbS for photovoltaic applications. *Nanotechnol. Rev.* **10**, 1484–1492 (2021)
- Muhammad, H.J., Siraj, A., Zhen-Yi, J., Muhammad, B.T., Muhammad, H.A., Shahroz, S., Abdullah, H.J., Muhammad, S.R.: First principal calculations to investigate structural, electronic, optical, and magnetic properties of Fe₃O₄ and Cd-doped Fe₃O₄. *Comput. Condens. Matter* **30**, 10222–10243 (2022)
- Muhammad, H.J., Muhammad, S.B.R., Mohd, Z.H., Bin, M., Ibrahim, A.S., Syed, Z.H.R., Mohd, A.B.A., Shahroz, S., Mohammed, A.A.: A comparative DFT study of Bandgap engineering and tuning of structural, electronic, and optical properties of 2D WS₂, PtS₂, and MoS₂ between WSe₂, PtSe₂, and MoSe₂ materials for photocatalytic and solar cell applications. *J. Inorg. Organomet. Polym.* **34**, 322–335 (2023)
- Mott, N.F., Davis, E.A.: *Electronics Processes in Non-Crystalline Materials*. Clarendon, Oxford (1979)
- Moraes, A., Andrade, P.F., Faria, A.F., Simões, M.B., Salomão, F., Barros, E.B., Gonçalves, M.D.C., Alves, O.L.: Fabrication of transparent and ultraviolet shielding composite films based on graphene oxide and Cellulose Acetate. *Carbohydr. Polym.* **123**, 217–227 (2015)
- Necula, A.M., Oлару, N., Oлару, L., Homocianu, M., Ioan, S.: Influence of the substitution degrees on the optical properties of cellulose acetates. *J. Appl. Polym. Sci.* **115**, 1751–1757 (2010)

- Numan, A., Jian-Min, Z., Shoaib, N., Muhammad, T.A., Shahroz, S., Umber, A., Noman, A., Muhammad, I., Rabia, L.: A comparative study of structural, vibrational mode, optical and electrical properties of pure nickel selenide (NiSe) and Ce-doped NiSe nanoparticles for electronic device applications. *Phys. B Condens. Matter* **649**, 414471–414493 (2023)
- Orelma, H., Hokkanen, A., Leppänen, I., Kammiovirta, K., Kapulainen, M., Harlin, A.: Optical cellulose fiber made from regenerated cellulose and cellulose acetate for water sensor applications. *Cellulose* **27**, 1543–1553 (2020)
- Pasha, S.K.K., Deshmukh, K., Basheer, A., Chidambaram, K., Mohanapriya, M.K., Raj, A.N.: Investigation of microstructure, morphology, mechanical, and dielectric properties of PVA/PbO nanocomposites. *J. Adv. Polym. Technol.* **36**, 352–361 (2015)
- Peng, J., Gao, W., Gupta, B.K., Liu, Z., Aburto, R.R., Ge, L., Song, L., Alemany, L.B., Zhan, X., Gao, G., Vithayathil, S.A., Kaiparettu, A., Marti, A.A., Hayashi, T., Zhu, J.J., Ajayan, P.M.: Graphene quantum dots derived from carbon fibers. *Nano Lett.* **12**, 844–849 (2012)
- Ramesan, M.T., Varghese, M., Jayakrishnan, P., Periyat, P.: Silver-Doped Zinc Oxide as a nanofiller for development of Poly(vinyl alcohol)/Poly (vinyl pyrrolidone) blend nanocomposites. *Adv. Polym. Technol.* **37**, 137–143 (2018)
- Ramakanth, K.: Basic of Diffraction and Its Application. I.K. International Publishing House Pvt. Ltd, New Delhi (2007)
- Radhika, T., Anju, K.R., Silpa, M.S., Ramalingam, R.J., Al-Lohedan, H.A.: Cellulose acetate/N-TiO₂ bio-composite flexible films with enhanced solar photochromic properties. *J. Electron. Mater.* **46**, 4567–4574 (2017)
- Sivacarendran, B., Sumeet, W., Manal, A., Emily, P.N., Jian, Z., Serge, Z., Sharath, S., Madhu, B., Kourosh, K.Z.: Field effect biosensing platform based on 2D α -MoO₃. *ACS Nano* **11**, 9753–9760 (2013)
- Shahroz, S., Muhamma, H.J., Azka, R., Muhammad, B.T., Muhammad, I.I., Zhen-Yi, J., Malik, R.Q., Abdul-Ahad, H., Ateeq, U.R., Abdullah, H.J., Abdullah, Y.A., Mohamed, A.S., Hessien, M.M.: Evaluation of structural, morphological, optical, and electrical properties of zinc oxide semiconductor nanoparticles with microwave plasma treatment for electronic device applications. *J. Mater. Res. Technol.* **19**, 2126–2134 (2022a)
- Shahroz, S., Muhammad, N.A., Sumaira, M., Umber, A., Rabia, L., Ali, A., Saqib, M., Vineet, T., Amnah, M.A., Moamen, S.R., Asad, A., Muhammad, A., Abid, Z.: Analysis and characterization of opto-electronic properties of iron oxide (Fe₂O₃) with transition metals (Co, Ni) for the use in the photodetector application. *J. Mater. Res. Technol* **25**, 6150–6166 (2023)
- Shahroz, S., Abdullah, H.J., Muhammad, H.J., Azka, R., Zahraa, H.K., Ali, H.A., Zunaira, G., Saba, A.R., Rami, A.P., Eman, A., Eng-Poh, N.G., Salit, M.S.: Enhancement in structural, morphological, and optical properties of copper oxide for optoelectronic device applications. *Nanotechnol. Rev.* **11**, 2827–2838 (2022b)
- Shahroz, S., Muhammad, I., Muhammad, Y.N., Shazia, S., Muhammad, A.M., Muhammad, A., Abdullah, S.A., Stanislaw, L., Jana, P., Saifur, R.: Investigating the impact of Cu²⁺ doping on the morphological, structural, optical, and electrical properties of CoFe₂O₄ nanoparticles for use in electrical devices. *Materials* **15**(10), 3502–3517 (2022c)
- Samsi, N.S., Zakaria, R., Hassan, O.H., Yahya, M.Z.A., Ali, A.M.M.: X-ray diffraction and infrared studies on plasticized cellulose acetate complexed with ammonium iodide for solid polymer electrolyte. *Mater. Sci. Forum* **846**, 523–527 (2016)
- Tagliente, M.A., Massaro, M.: Strain-driven (0 0 2) preferred orientation of ZnO nanoparticles in ion-implanted silica. *Nucl. Instrum. Methods Phys. Res. b* **266**, 1055–1061 (2008)
- Tanaka, K.: Optical properties and photoinduced changes in amorphous As-S films. *Thin Solid Films* **66**, 271–279 (1980)
- Vimala, D., Hashmi, S.Z., Upendra, K., Choudhary, B.L., Kuznetsov, A.E., Saurabh, D., Shalendra, K., Savas, K., Dolia, S.N., Alvi, P.A.: Spectroscopic studies, molecular structure optimization and investigation of structural and electrical properties of novel and biodegradable Chitosan-GO polymer nanocomposites. *J. Mater. Sci.* **55**, 14829–14847 (2020)
- Vimala, D., Hashmi, S.Z., Upendra, K., Choudhary, B.L., Saurabh, D., Dolia, S.N., Alvi, P.A.: Optical and electrical properties of biocompatible and novel (CS-GO) polymer nanocomposites. *Opt. Quant. Electron.* **53**, 1–13 (2021)
- Vahid, V., MehmetEmin, P., Hossein, B., OğuzOrhun, T., Recep, K., Muhammed, B., Alireza, K., Ismail, K.: Cellulose acetate in fabrication of polymeric membranes. *Chemosphere* **295**, 13391–13410 (2022)
- Wang, S.H., Han, M.Y., Huang, D.J.: Nitric oxide switches on the photoluminescence of molecularly engineered quantum dots. *J. Am. Chem. Soc.* **131**, 11692–11694 (2009)
- Wang, Y., Li, Z., Wang, J., Li, J., Lin, Y.: Graphene and graphene oxide: biofunctionalization and applications in biotechnology. *Trend Biotechnol.* **29**, 205–212 (2011)

- Wang, Y., Zhang, X., Luo, Z., Huang, X., Tan, C., Li, H., Logo, O., Zheng, B., Li, B., Huang, Y., Yang, J., Zong, Y., Ying, Y., Zhang, H.: Liquid- phase growth of platinum nanoparticles on molybdenum trioxide nanosheets: anenhanced catalyst with intrinsic peroxidase-like catalytic activity. *Nanoscale* **6**, 12340–12344 (2014)
- Wemple, S.H., DiDomenico, M., Jr.: Behavior of the electronic dielectric constant in covalent and ionic materials. *Phys. Rev. B* **3**, 1338–1351 (1971)
- Wemple, S.H.: Refractive-index behavior of amorphous semiconductors and glasses. *Phys. Rev. B* **7**, 3767–3777 (1973)
- Wongkrua, P., Thongtem, T., Thongtem, S.: Synthesis of h- and α - MoO_3 by refluxing and calcination combination: phase and morphology transformation, photocatalysis, and photosensitization. *J. Nanomater.* **2013**, 1–8 (2013)
- Yogamalar, R., Srinivasan, R., Vinu, A., Ariga, K., Bose, A.C.: X-ray peak broadening analysis in ZnO nanoparticles. *Solid State Commun.* **149**, 1919–1932 (2009)
- Yuan, L., Weng, X., Zhou, M., Zhang, Q., Deng, L.: Structural and visible-near infrared optical properties of Cr-doped TiO_2 for Colored cool pigments. *Nanoscale Res. Lett.* **12**, 597–598 (2017)
- Zak, A.K., Abd. Majid, W.H., Abrishami, M.E., Yousefi, R.: X-ray analysis of ZnO nanoparticles by Williamson-Hall and size-strain plot methods. *Solid State Sci.* **13**, 251–256 (2011)
- Zakir, Ç., Lütfi Bilal, T.: The role of molybdenum trioxide in the change of electrical properties of Cr/ MoO_3 /n-Si heterojunction and electrical characterization of this device depending on temperature. *Sens. Actuators A: Phys.* **328**, 112765–112794 (2021)
- Zeyada, H.M., El-Nahass, M.M., El-Zawawi, I.K., El-Menyawy, E.M.: Structural and optical properties of thermally evaporated 2-(2,3-dihydro-1,5-dimethyl-3-oxo-2-phenyl-1H-pyrazol-4-ylimino)-2-(4-nitrophenyl) acetoneitrilethinfilms. *J. Phys. Chem. Solids.* **71**, 867–873 (2010)
- Zeyada, H.M., EL-Nahass, M.M., EL-Shabaan, M.M.: Gamma-ray irradiation induced structural and optical constants changes of thermally evaporated neutral red thin films. *J. Mater. Sci.* **47**, 493–502 (2012)
- Zhang, J., Zhang, Y., Xu, K.W., Ji, V.: Young's modulus surface and Poisson's ratio curve for cubic metals. *J. Phys. Chem. Solids* **68**, 503–510 (2006)

Publisher's Note Springer Nature remains neutral with regard to jurisdictional claims in published maps and institutional affiliations.